# Thermal fertilization of the high-latitude northern forests

Junjie Liu[1,2*], Paul O. Wennberg[2*], Nick Parazoo[1], Yi Yin[2], Christian Frankenberg[2, 1]

[1.] Jet Propulsion Laboratory, Caltech, US

[2.] Caltech, US

*Correspondence to: junjie.liu@jpl.nasa.gov; wennberg@caltech.edu

## Key Points:

- 3/4 of the spatial variations in productivity of high-latitude northern forest can be explained by growing season mean temperature (GSMT).
- Substituting space for time, we estimate the increase in GSMT enhanced productivity and net carbon uptake by ~20% between 1960–2010.
- The calculated enhancement of net ecosystem exchange contributes 56–72% of the trend in the $CO_2$ seasonal cycle amplitude at high latitudes.

## Abstract

Since the 1960s, carbon cycling in the high-latitude northern forest (HLNF) has experienced dramatic changes: most of the forest is greening and net carbon uptake from the atmosphere has increased. During the same time period, the $CO_2$ seasonal cycle amplitude (SCA) has almost doubled. Disentangling complex processes that drive these changes has been challenging. In this study, we substitute spatial sensitivity to temperature for time to quantify the impact of temperature increase on Gross Primary Production (GPP), total ecosystem respiration (TER), the fraction of Photosynthetic Active Radiation (fPAR), and the resulted contribution of these changes in amplifying the $CO_2$ SCA over the HLNF since 1960s. We use the spatial heterogeneity of GPP inferred from solar-induced chlorophyll Fluorescence in combination with net ecosystem exchange (NEE) inferred from column $CO_2$ observations made between 2015 and 2017 from NASA's Orbiting Carbon Observatory -2. We find that three quarters of the spatial variations in GPP and in the fPAR absorbed by the HLNF can be explained by the spatial variation in the growing season mean temperature (GSMT). The long term hindcast captures both the magnitude and spatial variability of the trends in observed fPAR. We estimate that between 1960 and 2010, the increase in GSMT enhanced both GPP and the SCA of NEE by ~20%. The calculated enhancement of NEE due to increase in GSMT contributes 56–72% of the trend in the $CO_2$ SCA at high latitudes, much larger than simulations by most biogeochemical models.



## Plain Language Summary

The carbon cycling in the high-latitude northern forest has experienced dramatic changes during the last 5-6 decades along with temperature increase almost double that of the global mean temperature. Using observations, we quantify the impact of temperature increase alone on the changes of gross primary production, greenness, and $CO_2$ seasonal cycle amplitude. Our results show a dominant temperature effect on the changes of carbon cycle over the region. Our results

imply that an additional 2-5 °C temperature increase by 2100 (RCP6.0, *IPCC AR5*) would dramatically alter the distribution of tree species over the region: evergreen trees will invade the shrublands, and much of the evergreen forests will transition to deciduous trees. GPP over the region has the potential to double.

## 1 Introduction

The High-Latitude Northern Forest (HLNF, 50°N to 75°N) is composed of needle leaf trees (both evergreen and deciduous), deciduous broad-leafed trees, and shrubland (Figure 1). It is responsible for ~20% of global Gross Primary Productivity (GPP) (Tramontana et al., 2017; Jung et al., 2017). Over the region northward of 50 degrees, precipitation substantially exceeds evaporation due to moisture convergence by the largescale eddy circulation, which results in a generally well-watered, thermally-limited ecosystem (Nemani et al., 2003). The northern extent of the forest is limited by the Arctic ocean and/or where summertime temperatures are too low. Because of its seasonality (days with nearly 24 hours of sunlight followed by days with 24 hours of darkness), uptake and release of carbon from the atmosphere is responsible for a large fraction of the seasonal cycle amplitude (SCA) in atmospheric $CO_2$. Without the HLNF, the SCA of $CO_2$ in the northern hemisphere would be only about half as large (Graven et al., 2013).

Since the 1960s, carbon cycling in the HLNF has experienced dramatic changes: most of the forest is greening (Zhu et al., 2016; Keenan and Riley, 2018) and net carbon uptake from the atmosphere has increased (Ciais et al., 2019). Although the underlying processes driving these trends are uncertain (Randerson et al., 1997; Zeng et a., 2014; Gray et al.,2014; Forkel et al., 2016; Piao et al., 2018; Bastos et al., 2019), it is generally agreed that both the increase in temperature and $CO_2$ are responsible (Randerson et al., 1997; Forkel et al., 2016; Piao et al., 2018; Bastos et al., 2019). Global mean $CO_2$ concentration has increased from 320ppm in 1958 to ~400 ppm in 2010s (https://www.esrl.noaa.gov/gmd/ccgg/trends/). Plants generally grow faster as $CO_2$ increases, which is called $CO_2$ fertilization (Kimball et al., 1983; Long et al., 2004). The optimal temperature for plants growth is higher than the mean annual temperature over high-latitude biomes (Huang et al., 2019), thus, we expect that increase in temperature accelerates plants growth, unlike tropics

where the increase in temperature can suppress growth (Sullian et al., 2020). The temperature increase over the NH high latitudes is nearly double that of the mean temperature increase over land (IPCC AR5). In a parallel framing to $CO_2$ fertilization, we call increase of productivity due to thermal dynamical effect as "thermal fertilization". Quantifying the individual role of temperature and $CO_2$ increases on plants growth and net carbon uptake is crucial for projecting future climate change (Friedlingstein et al., 2014). However, because the temporal changes in temperature and $CO_2$ have been so correlated, disentangling their individual contribution with observations is difficult, especially over HLNF where conventional observations are sparse (Schimel et al., 2015). Previous studies primarily make use of factorial simulations of biogeochemical models to isolate the impact of change in climate from other factors (e.g., Bastos et al., 2019). Studies using observation constraint are scarce to none.

In this study, we provide observation constraint on the impact of temperature change on Gross Primary Production (GPP), total ecosystem respiration (TER), and the resulting net ecosystem exchange (NEE) of the HLNF. We use the spatial heterogeneity of GPP inferred from solar-induced chlorophyll Fluorescence (SIF) (Frankenberg et al., 2011) in combination with NEE inferred from column $CO_2$ observations made between 2015 and 2017 from NASA's Orbiting Carbon Observatory -2 (OCO-2) (Crisp et al., 2017; Eldering et al., 2017). OCO-2 provides unprecedented spatial coverage of column $CO_2$ and SIF during this period.

Substituting the observed spatial-sensitivity of GPP and TER to temperature for time, we estimate the change in carbon cycling in the HLNF between 1960s and 2010s due to the warming this region has experienced. We diagnose what contribution these changes have made to the observed increase

in the $CO_2$ seasonal cycle amplitude (SCA) between 1958-1963 (International Geophysical Year (IGY) aircraft campaign) (Keeling et al., 1968) and 2009-2011 (Hiaper Pole-to-Pole observations (HIPPO) aircraft campaign) (Wofsy et al., 2011), and over NH high latitude $CO_2$ flask sites with long-record (>25 years) (Alert (Canada), Cold Bay (Alaska, US), Barrow (Alaska, US), and Shemya Island (Alaska, US)). To evaluate whether space and time can be substituted, we compare the trend and interannual variability in fPAR calculated with this assumption to observations of the changes in GIMMS3g fPAR (Zhu et al., 2013) over space and time.

## 2 Materials and Methods

We calculate monthly mean GPP (2.1) and NEE (2.2) for 2015–2017 with OCO-2 SIF and column $CO_2$ retrievals, respectively. TER is calculated as the difference between NEE and GPP (2.2). We substitute seasonal (i.e., spring, summer, and fall (2.3)) spatial GPP–T and TER–T relationship for time to predict the temporal changes of GPP and TER and the resulting changes in NEE from increase in temperature for the time period of 1980–2011 and between 1958-1963 and 2009-2011 (2.4). To evaluate the space-for-time substitution, we compare predictions of the change in fPAR between 1982 and 2012 based on the modern spatial fPAR–T relationship with the changes in GIMMS3g fPAR (2.4). Finally, we calculate the $CO_2$ seasonal cycle amplitude (SCA) changes due to changes in NEE between 1958–1963 and 2009–2011 and for the time period of 1980–2011 (2.5).

### 2.1 Solar Induced chlorophyll Fluorescence (SIF) – constrained monthly mean GPP calculation

We use SIF retrieved from OCO-2 to calculate monthly mean GPP. SIF is fluorescence from plants that occurs during photosynthesis. It is sensitive to both plant structure and photosynthetic function, and is linearly correlated with GPP under high-light conditions (Frankenberg et al., 2011;

Sun et al., 2018). OCO-2 SIF retrievals have footprint size ~1.2 x 2 $km^2$. Each SIF retrieval is scaled based on solar zenith angle, date, latitude, and local passing time, ~ 1:30pm, to produce a daily mean (Frankenberg et al., 2011). The monthly mean value at each 4° x 5° grid is a simple averaging of the daily mean SIF values. The 4° x 5° spatial resolution is chosen for the consistency with the optimized NEE from top-down atmospheric $CO_2$ flux inversion. We use OCO-2 level 2 SIF observations from land nadir mode only between Jan 2015 and Dec 2017. The time frame is constrained by the availability of the FLUXCOM GPP product, an upscaling GPP product based on GPP from flux towers, ancillary satellite, and meteorology (Tramontana et al., 2016; Jung et al., 2017).

The growing season mean SIF value increases exponentially with temperature over the grid points with tree cover larger than 40% (Figure S1). The SIF–temperature sensitivity is within the sensitivity range of the three FLUXCOM GPP products (Figure S1). There is no obvious discontinuity in the sensitivities of both SIF and FLUXCOM GPP products to temperature, so we calculate monthly mean GPP over 50°N-75° N at 4° x 5° spatial resolution as the product of OCO-2 SIF and a scaling factor derived using the growing season (GS) mean GPP from three FLUXCOM products and mean SIF. The scaling factor, 22.9 ± 2.6 (gram carbon micron sr per day per watts (gC μm sr $day^{-1}$ $W^{-1}$)), is consistent with (Sun et al., 2018). In using the same conversion factor across the region, we have assumed that different tree types have the same relationship between SIF and GPP (see Section 4).

**2.2 Top-down NEE estimation with CMS-Flux and Total Ecosystem Respiration (TER) calculation during 2015 and 2017**

We optimize monthly mean NEE with CMS-Flux system (Liu et al., 2014; 2017; 2018; Bowman et al., 2017) at each 4° x 5° grid with OCO-2 B9 land nadir observations (Eldering et al., 2017), which span from Sep 2014–April 2018. For readers interested in more details on atmospheric $CO_2$ flux inversion, please refer to (Liu et al., 2014; 2015; 2017). The prior fluxes include climatology terrestrial biosphere carbon fluxes from CASA-GFED 3 (Randerson et al., 1997), biomass burning from GFED4, fossil fuel emissions from ODIAC (Oda et al., 2018), and ocean carbon fluxes from ECCO-Darwin (Menemenlis et al., 2008). Except the climatology terrestrial biosphere fluxes from CASA-GFED3, the other types of carbon fluxes are yearly dependent. We calculate TER as the difference between the optimized NEE and GPP between 2015–2017. The right three panels in Figure S2 show the dependency of TER on temperature during the three growing season. The estimated TER shows strong dependence on temperature, which is expected, since TER's two components, autotropic and heterotrophic respiration, depend on the amount of carbon fixed through photosynthesis (Baldocchi, 2008). In Figure S2, we remove points that have nonphysical negative TER values.

We validate the top-down flux inversion results by comparing the $CO_2$ SCA sampled at Mauna Loa against observed $CO_2$ SCA, and comparing posterior $CO_2$ concentrations between April and September against independent aircraft $CO_2$ observations north of 30°N. The SCA of posterior $CO_2$ concentration sampled at Mauna Loa is within the uncertainty range of the observed $CO_2$ SCA (Figure S3). The random error and bias of regional mean monthly posterior $CO_2$ concentration is 0.4 ppm and 0.1 ppm, respectively (Figure S3) (Supplementary Text).

**2.2 Definition of growing season**

We define spring, summer, and fall with SIF-optimized GPP product (Parazoo et al., 2014), which optimally combines OCO-2 SIF observations with climatology mean state from TRENDY models (Sitch et al., 2015). The product maintains essentially the same seasonality as original SIF observations during growing season, while filling the observation gaps during the late growing season and winter. At each grid point, the growing season is defined as the time period when the GPP values are larger than 20% of the maximum GPP at that grid point. Spring and fall are defined as the time period when GPP is between 20% and 75% of maximum GPP, and summer is the time period between spring and fall. We choose 20% as the threshold to ensure that the plants have started growing and the start of the spring is well-defined. We find that 10% of grid points would have no spring if the threshold is 30% instead of 20%, since GPP increases sharply during spring over Eurasia.

**2.4 Prediction of growing season monthly mean GPP, TER, and fPAR**

We substitute the spatial sensitivity to temperature for time to predict the temporal changes in GPP, TER, and fPAR due to changes in temperature. Note that the spatial $CO_2$ gradient is typically less than 10 ppm and so all plants are growing at any time experience the same [CO2]. Our approach of substitution of space-for-time to predict changes in carbon states due to climate has been used by others. For example, Sullivian et al. (2020) predicted changes in tropical biomass from changes in temperature using the spatial biomass–temperature sensitivity. Figure S4 shows that the fPAR – T spatial sensitivity is relatively constant, with variability less than 5%, implying that the spatial sensitivity to temperature represents a semi-equilibrium state. We use the spatial – temperature sensitivity shown in Figure S2 and S4 to predict temporal changes of GPP, TER, and fPAR.

In predicting GPP, we use GPP/PAR – T spatial sensitivity (Figure S2) to calculate the temporal changes of GPP/PAR with changes in temperature, and then multiply PAR to get final GPP prediction. Since PAR is only a function of latitude and seasons, we use the same PAR averaged over 2015-2017 to calculate GPP.

With the spatial – temperature sensitivity derived from the observation-constrained GPP and TER between 2015 and 2017 and CRU monthly mean air temperature during 2009-2011 and 1958-1963, we predict the monthly GPP and TER during growing season of these two time periods (Figure S6). In predicting the GPP for 2009-2011 and 1958-1963 time periods, we assume that the temporal range of the three growing seasons is the same as in 2015-2017, which is a reasonable assumption since the temporal resolution of our study is month and the growing season length only increases by ~0.25 month for every ~1 degree increase of temperature (Figure S7). We generate 10-member ensemble GPP and TER predictions with the 95% confidence interval shown in Figure S2. We calculate the uncertainty from the ensemble GPP and TER hindcasts shown in Figure S6.

We calculate NEE during growing season as the difference between ensemble TER and GPP, and assume that non-growing season NEE is proportional to the growing season NEE (Kauppi and Posch, 1985). The proportional assumption may be a conservative estimation of non-growing season NEE changes (see Section 4).

To calculate NEE between 1980 to 2011, we predict growing season GPP and TER with four-year frequency, where we use monthly mean temperature averaged over every four years. We find that the results are not sensitive to the prediction frequency. In total, we have eight groups of NEE

hindcast between 1980 and 2011. We choose 2011 as the ending year to be consistent with the time frame of HIPPO aircraft campaign.

With the same seasonally-dependent GPP/PAR – T spatial sensitivity and monthly mean temperature, we predict monthly mean GPP between 1960 and 2014. Following the same method described above, we predict monthly mean fPAR with the seasonally-dependent relationship calculated for 2013-2016 (Figure S5). The sensitivity shown in Figure S5 is based on fPAR from GIMMS3g. Since fPAR from GIMMS3g has more than 30-year record, the trend calculation is more robust than that is based on MODIS. In the main text, we use fPAR from GIMSS3g in trend calculation, but use fPAR from MODIS in Figure 2, since MODIS has higher spatial resolution than AVHRR used in the earlier record of GIMMS3g (https://nsidc.org/support/21524371-What-are-the-MODIS-sensor-s-strongest-attributes-and-how-do-they-compare-to-other-sensors-).

### 2.5 $CO_2$ simulations with GEOS-Chem transport model

We use GEOS-Chem transport model to simulate a 3-hourly 10-member ensemble of $CO_2$ concentrations with the predicted ensemble monthly NEE (i.e., TER-GPP) as boundary conditions during 1958-1963 (IGY), 2009-2011 (HIPPO) and the monthly NEE from 1980 to 2011. We assume the same diurnal biosphere fluxes during these two time periods, which are from CASA-GFED3.

We run GEOS-Chem transport model at 2° x 2.5° spatial resolution driven by MERRA2 reanalysis after regridding 4°x5° NEE to 2°x2.5° spatial resolution. The transport model has smaller transport errors over high latitudes at 2° x 2.5° resolution than at 4° x 5° resolution. For both IGY and HIPPO

$CO_2$ simulations, we run ensemble transport model simulations continually from 2006 to 2011, and we then analyze $CO_2$ simulation results over the last three-year simulation. The difference between IGY and HIPPO $CO_2$ simulations is only from the boundary forcing, not from the meteorology forcing. For each of the eight-group NEE from 1980 to 2011, we run ensemble transport model simulations continually for six years with meteorology from 2006 to 2011, and then analyze $CO_2$ simulation results for each group over the last three-year simulation. As a result, the changes of $CO_2$ SCA are only due to changes of NEE, not due to changes of transport**.** We follow the same method described in Graven et al. (2013) (Supplementary Text) to calculate $CO_2$ SCA for both surface sites and aircraft observations and the corresponding model simulations.

## 3 Results

### 3.1 The spatial GPP – temperature relationship

Over the HLNF, both the spatial distribution and seasonal evolution of GPP closely follow those of temperature (Figure 1). From April to July, increases in SIF propagate from the west to the east of each continent following the spatial increase of monthly mean temperature (Figure S8). From July to October, GPP decreases as cooler temperature propagates from the east to the west of each continent (Figure S8). The spatial changes illustrate how the onset and length of growing season (GS) are closely coupled to the surface temperature (Figure S7). The growing season length increases ~one week with each degree increase in surface temperature, consistent with Park et al. (2016).

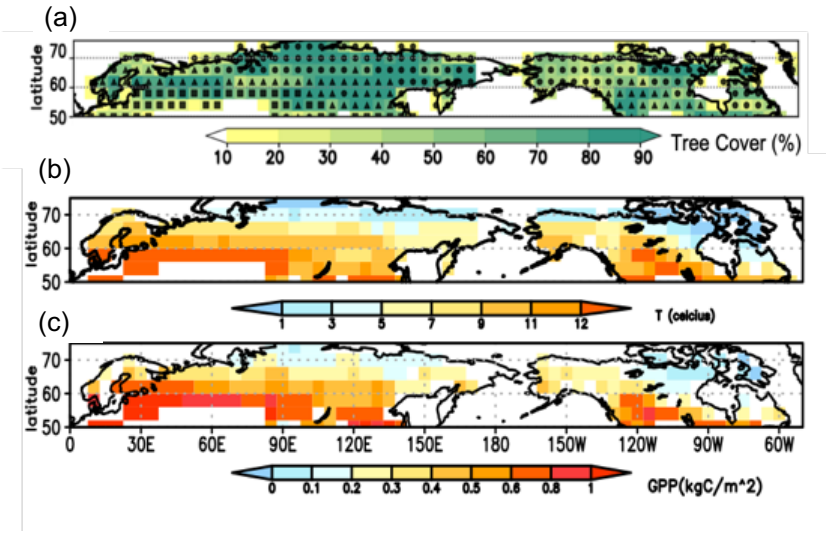


Figure 1 **Temperature controls on the spatial distribution of gross primary production (GPP) over high latitude northern forest (50°N – 75°N).** (a). Tree percentage and dominant tree types at every 4° x 5° grid. Dots: shrubland; triangles: needleleaf forest; and squares: deciduous boreal forest. The tree type is based on condensed MODIS International Geosphere Biosphere Program (IGBP) map. (b). Mean temperature (unit: °C) between April and September over 2015-2017. (c). Mean GPP (unit: kgC/m$^2$) integrated between April and September over 2015-2017. The temperature is 2-meter air temperature from ERA-interim reanalysis (Table S1). GPP is scaled SIF.

Quantitatively, the spatial variation in GSMT explains 70% of GPP/PAR (Photosynthetic Active Radiation) variability (Figure 1b and c and Figure 2a) (and 75% of the variability in GPP, Figure S9). The ratio between seasonally-averaged GPP and the seasonally-averaged PAR removes the influence of the somewhat larger solar flux at lower latitude. While PAR is a function of latitude over this domain, it contributes less than 10% to the GPP – temperature spatial relationship (Figure S9). The correlation between GPP/PAR and GS mean temperature is not simply due to variations in latitude: trees growing at the same latitude have large variability in productivity due to the longitudinal-variation in GSMT. For example, at 62° ± 2° N latitude (highlighted by closed circles in Figure 2a), GPP/PAR varies from 0.10 to 0.45 gram carbon per mega Joules (gC MJ$^{-1}$), highly correlated with the variation in GSMT.

The distribution of vegetation cover is also highly correlated with GSMT (Figure 2a). The mean GS temperatures are 9.2°C, 11.5°C, and 13.6°C for shrubland, needleleaf forest, and deciduous boreal forest, respectively. Between the transitional zones, mixed forest types co-exist. The correlation is illustrative of the complex role that temperature likely plays on many aspects of the ecology of the HLNF. From this correlation, we might anticipate that warming would lead to succession of the dominant trees in a fashion consistent with the patterns observed spatially (e.g. evergreen forests will transition to deciduous forests as the GSMT reaches 13°C). Limited field measurements are consistent with this hypothesis (Kharuk et al., 2007; Bjorkman et al., 2018).

Why is GPP/PAR so sensitive to temperature in the HLNF? GPP/PAR is a product of amount of the fraction of PAR absorbed by plants (fPAR) and the light use efficiency (the efficiency of conversion of absorbed sunlight to assimilated carbon) (Farquhar et al., 1980). The fPAR reflects forest structure (leaf area index, LAI) and is observed to increase with temperature in the HLNF (Zhu et al., 2016) (Figure 2b). The fraction of absorbed sunlight resulting in fixation of $CO_2$ (light use efficiency) depends on, among other things, plant functional types. Field experiments (Ahl et al., 2004) show that the light use efficiency of deciduous forest is ~30% higher than needle leaf trees, consistent with the behavior seen in Figure 2c. In the absence of water or nutrient limitations, light use efficiency is also expected to increase with temperature in cold forests (Figure 2c) (Horn and Schulz, 2011). Due to the high rates of precipitation and snow melt, water limitations – especially earlier in the growing season – are not expected. As shown in Figure S10, GPP increases with the increase in vapor pressure deficit, opposite to the expected relationship for water-limited ecosystems. Because the rate of nitrogen fixation also increases rapidly with temperature (Schimel et al., 1997; Welter et al., 2015), nitrogen limitation may not change as plants increase their

demand as temperature increases. Thus, the sensitivity of GPP/PAR to GSMT results from the sensitivity of both forest structure (fPAR) and light use efficiency, with similar contributions (0.090 vs. 0.100) from each (Figure 2 b and c).

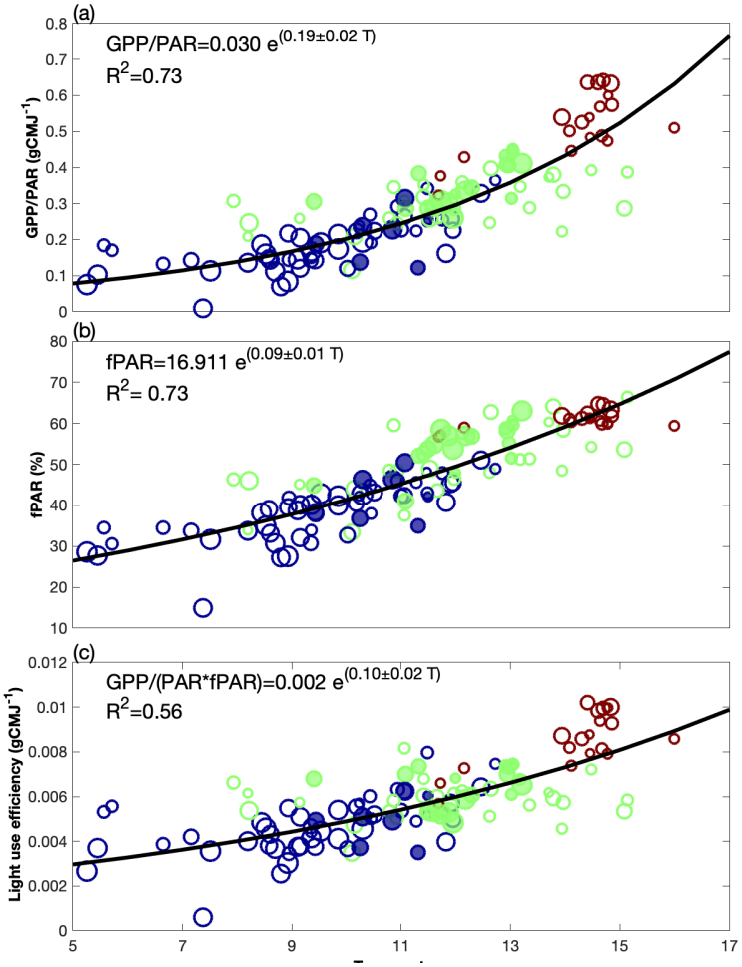


Figure **2 The spatial relationship between temperature and Gross Primary Production (GPP) and its contributing factors between 50°N and 75°N.** The x-axis is the growing season mean temperature, GSMT. (a) GSMT vs. the ratio between GPP and photosynthetic active radiation (PAR) (unit: gram carbon per mega Joules (gC $MJ^{-1}$); (b) GSMT vs. fraction of Photosynthetic Active Radiation absorbed by the forest (fPAR) (%); (c) temperature vs. light use efficiency (unit: gC $MJ^{-1}$). Green: needleleaf forest; brown: deciduous boreal forest; blue: shrubland; The size of circles is proportional to the percentage of tree coverage. Filled circles are the points with latitude equal to 62°N. The minimum of tree coverage for each type is 40%. The uncertainty is 3σ of the fitting. The temperature 2-meter air temperature from ERA-interim reanalysis (Table S1)

### 3.2 Hindcast of the fPAR and GPP/PAR from the changes in GSMT since 1960

With more than 30-year (1982-2016) of fPAR record from GIMMS3g (Zhu et al., 2013), we can test how well the temporal change in fPAR is explained by the observed spatial temperature

sensitivity. We find that the modern correlation of fPAR with GSMT accurately captures the variability and trend in fPAR over the past several decades. Remarkably, even the interannual variations in fPAR (Figure 3) are well predicted by the spatial fPAR – T correlations, with $R^2$ between observation and predicted fPAR equal to 0.62 (Figure 3d). The calculated temporal trend of fPAR during the period of fPAR observation is 0.29 ± 0.08 %/year, somewhat larger than the observed fPAR trend (0.20 ± 0.06 %/year). The larger trend in the GS fPAR hindcast results primarily from an over-prediction of the trends in the fall (Figure S11). The hindcast fPAR trend calculated from1960-2014 is 0.20 ± 0.06 %/year, consistent with the observed fPAR trend between 1982 and 2014. Figure 3d indicates that the current spatial correlation between fPAR and GSMT can explain the historical changes in HLNF mean fPAR without invoking a significant role for $CO_2$ fertilization .

The hindcast of fPAR also captures the spatial inhomogeneity in the observed fPAR changes. Between 2007-2011 and 1983-1987, the northeast Eurasia and western Europe have experienced larger increases in GSMT than North America (NA) (Figure 3a). The changes in both the observed and hindcast GS fPAR show similar spatial pattern as the temperature differences between these two time periods (Figure 3b and c). This, again, is consistent with temperature playing the dominant role in controlling fPAR. For example, if $CO_2$ fertilization was responsible for enhanced fPAR, we would not expect the fractional change to be so well correlated with the spatial change in temperature given that the change in $CO_2$ was identical across both space and time. The overestimate in the calculated fPAR changes over NA may be caused by the land cover changes from disturbance (Wang et al., 2019) that the hindcast does not consider.

The trend in the hindcast GPP during GS is 0.36 ± 0.07%/year, about two times the hindcast fPAR trend during 1960-2014, consistent with Figure 2 showing that only half of the GPP/PAR – T spatial sensitivity is attributed to change in fPAR. The trend in GPP during spring is larger than the other two seasons (0.44% ± 0.09% vs. 0.34% ± 0.08% and 0.34% ± 0.10%) (Figure S11), as a result of the both larger increase in temperature and higher sensitivity of GPP/PAR to temperature in spring (Figure S2).

Only nine tower sites in *FLUXNET 2015* data archive (https://fluxnet.fluxdata.org/about/) have record longer than 15 years between 50°N and 75°N, mostly over Europe. The sparseness of the *FLUXNET 2015* over the region limit the ability of using FLUXNET GPP to evaluate GPP – T spatial relationship and the temporal changes of GPP with time.

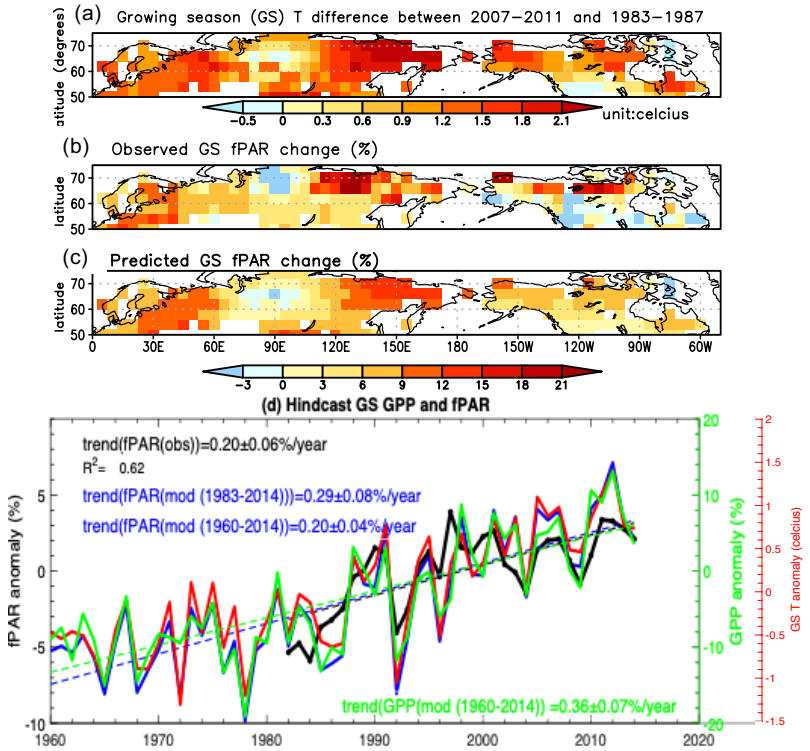


Figure 3. **Annual hindcast of GPP and fPAR between 1960 and 2014**. (A) Growing season (GS) mean temperature changes between 2007-2011 and 1983-1987. (B) Observed growing season fPAR change (%) between 2007-2011 and 1983-1987. (C) Hindcast growing season fPAR change (%) between 2007-2011 and 1983-1987 calculated from the fPAR-T spatial relationship (SI Appendix, Figure S13). (D) Annual fPAR and GPP anomaly and trend. Black:

observed fPAR anomaly and trend (dashed line); blue: hindcast fPAR anomaly and trend (%); green: hindcast GPP anomaly (%) and trend (dashed line); red: GS temperature anomaly. The mean values for each variable are the average between 1983 and 2014. The uncertainty is 3σ of the linear fitting. The fPAR observations are from GIMMS3g. The temperature is from Climatic Research Unit (CRU) (Table S1)

### 3.3 The impact of thermal fertilization on the NH $CO_2$ seasonal cycle amplitude

The increase of GPP would have increased both net carbon uptake during growing season and net carbon release during non-growing season (due to increased carbon pool size and increases in the rate of ecosystem respiration with temperature) (Zhao et al., 2014). As a result, it is expected that the increase in temperature would have enhanced the SCA of NEE. In turn, the increase of NEE SCA may have contributed to the documented large increase of NH $CO_2$ SCA (Graven et al., 2013). Between 1960 and 2010, the GPP and TER are calculated to have increased 20 ± 12% and 18 ± 12%, respectively, between April and Sep (Figure S6). The NEE between April and Sep increased by 23 ± 12%. The NEE amplitude, which is defined as the difference between the net source and net sink, increases by 21 ± 8% over 50°N-75°N (Figure S6).

We sample the $CO_2$ concentrations along the IGY and HIPPO aircraft locations, respectively, in the mid-troposphere (~500 hPa) and those four high latitude sites. Figure S12 summarizes the $CO_2$ SCA changes from observations and predictions. The change in GSMT is estimated to contribute 19-42% of the total observed $CO_2$ SCA changes north of 45°N between two aircraft campaigns, and 34 -76% of the $CO_2$ SCA change due to changes in carbon cycling in the HLNF (Figure 4). At the four surface sites, increase in the GSMT is calculated to contribute 56 - 72% of the observed trends in the $CO_2$ SCA (Figure 4).

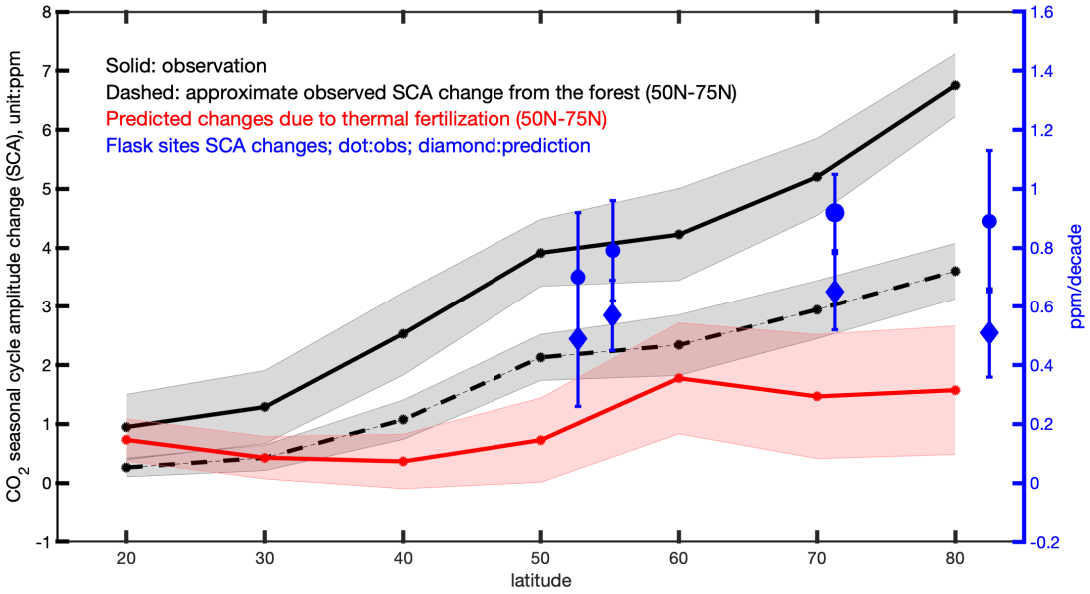


Figure 4 **Temperature driven change of NH $CO_2$ seasonal cycle amplitude.** Solid black line: the observed $CO_2$ seasonal cycle amplitude (SCA) changes between HIPPO (2009-2011) and IGY (1958-1963) aircraft campaigns at 500 hPa. Dashed black line: the approximate $CO_2$ SCA change between HIPPO and IGY at 500 hPa attributed to the HLNF. Red: the calculated $CO_2$ SCA changes due to the temperature increase of the HLNF. Blue: observed (solid dot) and predicted (diamonds) $CO_2$ SCA trend (unit: ppm/decade) at Shemya Island (Alaska, US) (52.71°N), Cold Bay (Alaska, US) (55.2°N), Barrow (Alaska, US) (71.3°N), and Alert (Canada) (82.4°N). The observation source is listed in Table S1.

## 4 Discussion

Though the predicted changes in carbon cycling in the HLNF is supported by the fPAR observations, further study is needed to test some assumptions used in the study. We have assumed a single scaling factor between the observed SIF and GPP. While this assumption is supported by (Sun et al., 2018; Li et al., 2018), it requires additional testing within these biomes. In particular, about 50% of the observed correlation between SIF and temperature is not explained by fPAR, but by the "*light use efficiency*". The estimated change in light use efficiency is correlated with biome (evergreen vs. shrub vs. deciduous trees, Figure 2c) and further work is needed to test whether all the differences in SIF of these biomes is indeed related to the differing photosynthetic efficiency of these tree types or may (partially) reflect differences the optics of SIF within canopies differing in structure.

Though studies show that the magnitude of non-growing season NEE is positively correlated with GS NEE *(*Yuan et al., 2011*),* the assumption that the change in non-growing season NEE is proportional to the changes in GS NEE may not always be valid. In using this assumption, we have ignored the impact of changes of snow coverage and freezing/thaw on ecosystem respiration (Natali et al., 2019) and nonhomogeneous changes in temperature throughout the year. There is evidence that the rate of respiration outside the GS may have increased faster than during GS because of larger temperature increase during fall and winter (Schuur et al., 2015).

The rapid increase in GPP with GSMT is certainly limited: the data shown in Figure 2 extends only to a GSMT of 16°C. It is expected that at some point, photosynthetic, water, and other nutrient limitations will limit further increase in GPP with temperature, especially during summer. Even today there is evidence that by mid/late summer such limitations come into play. In addition, the increase in abiotic (e.g. fire) and biotic (e.g. herbivory) disturbance with climate will also impact productivity.

Despite the limitations noted above, the spatial variations in fPAR and GPP in the HLNF are remarkably well correlated with temperature (Figure 2 and Figure S1), consistent with a thermally-limited ecosystem. The strong temperature control on changes in fPAR and GPP and its large contributions to changes in $CO_2$ SCA are in contrast to results obtained from most (Piao et al., 2018; Bastos et al., 2019), but not all biogeochemical models (Forkel et al., 2016), which generally suggest a dominant $CO_2$ fertilization effect on changes on NEE in the HLNF (and thereby the $CO_2$ SCA). The high degree of spatial correlation between fPAR, GPP, and GSMT provides a key observational measure that can be used to evaluate and improve upon corresponding model simulated properties. A factorial simulation with changes only in temperature drivers for

biogeochemical models will be able to isolate temperature effect from other factors, and thereby test the model behavior against observations to identify possible model deficiencies.

That warming alone accounts for nearly all the observed fPAR trend is in agreement with prior observational studies that suggest $CO_2$ fertilization is not a major contributor to carbon exchange in mature forests (Jiang et al., 2020) and, more broadly, in the boreal (Girardin et al., 2011). Over mature forest, even under warmer climate (when $CO_2$ fertilization is expected to contribute much more than in cooler climates), GPP increases ~12% with 150 ppm $CO_2$ enrichment (Jiang et al., 2020). Extrapolating the results in Jiang et al. (2020), the ~80 ppm increase in $CO_2$ between 1960s and 2010s implies a ~6% increase of GPP over boreal forest, where a large proportion of forests is undisturbed, especially over Eastern and Northern Canada and Eurasia (https://daac.ornl.gov/NACP/guides/NA_Tree_Age.html). Since fPAR accounts for half of GPP increases, fPAR may only increases by ~3% from $CO_2$ fertilization between 1960s and 2010, well within the uncertainty estimates shown in Figure 3. The more important role of temperature implied by the current spatial dependence of fPAR on GSMT is consistent with thermal fertilization explaining most of the temporal trend in fPAR.

The ensemble of CMIP5 models suggest that by 2100, absent of efforts to mitigate climate forcing, these forests will experience an additional 2-5 °C increase relative to 1986-2005 (RCP6.0, *IPCC AR5*) in GSMT. Figure 2 implies that such a change would dramatically alter the distribution of tree species over the region: evergreen trees will invade the scrublands all the way to the Arctic ocean, and much of the current evergreen forests will transition to deciduous trees. GPP over the region has the potential to double.

## 5. Conclusion

Three quarters of the spatial variations in gross primary production and fPAR over high-latitude northern forest can be explained by the spatial variation in growing season mean temperature. Substituting observed spatial sensitivity to temperature for time, we estimate the change in carbon cycling in the HLNF between 1960s and 2010s, and diagnose what contribution these changes have made to the observed increase in the $CO_2$ SCA. The hindcast captures both the magnitude and spatial variability of the trends in observed fPAR. We calculate that the observed high-latitude warming results in a 20 ± 12% and 18 ± 12% increase in GPP and TER, respectively, during growing season. The calculated changes in GPP and TER result in an increased seasonality of NEE by 21 ± 8% between the 1960s and 2010s. In turn, the increase of the NEE SCA contributes 56-72% of the observed increase in the $CO_2$ SCA at high latitude continental surface sites and 17-43% of the observed change in the SCA in the mid-troposphere.

### Data Availability

The sources of all the data used in this paper are listed in Table S1.

### Acknowledgments

We appreciate constructive comments and suggestions from James Randerson, Dave Schimel, and TRENDY modelers (Stephen Sitch, Pierre Friedlingstein, Vivek Arora, Atul Jain, Markus Kautz, Danica Lobardozzi, Sebastian Lienert, Julia Nabel, Benjamin Poulter, Nicolas Vuichard, Andy Wiltshire, and Ning Zeng) in preparing this paper. Resources supporting this work were provided by the NASA High-End Computing (HEC) Program through the NASA Advanced Supercomputing (NAS) division at Ames Research Center. All authors declare no financial conflicts of interest. We acknowledge the funding support from NASA Carbon Cycle Science program and OCO-2/3 Science Team program. Part of the research was carried out at Jet Propulsion Laboratory, Caltech.

## References


1. Ahl, D. E., Gower, S. T., Mackay, D. S., et al. (2004). Heterogeneity of light use efficiency in a northern Wisconsin forest: Implications for modeling net primary production with remote sensing, *Remote Sens. Environ.*, **93**, 168– 178.
2. Baldocchi, D. D. (2008). Turner Review no. 15. "Breathing" of the terrestrial biosphere: Lessons learned from a global network of carbon dioxide flux measurement systems. *Aust. J. Bot.* **56**, 1. doi:10.1071/BT07151
3. Bastos, A., Ciais, P., Chevallier, F., et al. (2019). Contrasting effects of $CO_2$ fertilization, land-use change and warming on seasonal amplitude of Northern Hemisphere $CO_2$ exchange, *Atmos. Chem. Phys.,* **19**, 12361–12375 (2019), https://doi.org/10.5194/acp-19-12361-2019.
4. Bjorkman, A. D., Myers-Smith, I. H., Elmendorf, S. C., et al. (2018). Plant functional trait change across a warming tundra biome. *Nature*, **562**, 57-62. https://doi.org/10.1038/s41586-018-0563-7
5. Bowman, K. W., Liu, J., Bloom, A. A., et al. (2017). Global and Brazilian carbon response to El Niño Modoki 2011–2010. *Earth and Space Science*, 4, 637–660. https://doi.org/10.1002/2016EA000204
6. Ciais, P., Tan, J., Wang, X., et al. (2019). Five decades of northern land carbon uptake revealed by the interhemispheric $CO_2$gradient. *Nature*, **568** (7751), 221– 225.
7. Crisp, D., Pollock, H. R., Rosenberg, R., et al. (2017). The on-orbit performance of the Orbiting Carbon Observatory-2 (OCO-2) instrument and its radiometrically calibrated products, *Atmos. Meas. Tech*., 10, 59–81 (2017). https://doi.org/10.5194/amt-10-59-2017.
8. Eldering, A., Wennberg, P. O., Crisp, D., et al. (2017). The Orbiting Carbon Observatory-2 early science investigations of regional carbon dioxide fluxes. Science**, 358**, eaam5745.
9. Farquhar, G. D., von Caemmerer, S., Berry, J. A. (1980). A biochemical model of photosynthetic $CO_2$ assimilation in leaves of C 3 species. *Planta,* **149**, 78–90 (1980).
10. Forkel, M., Carvalhais, N., Rodenbeck, C., et al. (2016). Enhanced seasonal CO2 exchange caused by amplified plant productivity in northern ecosystems. *Science*, **351,** 696–9.

11. Frankenberg, C., Fisher, J. B., Worden, J., et al. (2011). New global observations of the terrestrial carbon cycle from GOSAT: Patterns of plant fluorescence with gross primary productivity, *Geophys. Res. Lett.*, **38**, L17706. doi:10.1029/2011GL048738.

12. Friedlingstein, P., Meinshausen, M., Arora, V. K., Jones, C. D., Anav, A., Liddicoat, S. K., Knutti, R. (2014). Uncertainties in CMIP5 Climate Projections due to Carbon Cycle Feedbacks. *J. Climate,* **27**, 511–526. https://doi.org/10.1175/JCLI-D-12-00579.1

13. Girardin, M. P., Bernier, P. Y., Raulier, F., Tardif, J. C., Conciatori, F., and Guo, X. J. (2011). Testing for a $CO_2$ fertilization effect on growth of Canadian boreal forests, *J. Geophys. Res.*, 116, G01012, doi:10.1029/2010JG001287.

14. Gray, J. M., Frolking, S., Kort, E. A., et al. (2014). Direct human influence on atmospheric $CO_2$ seasonality from increased cropland productivity. *Nature,* **515**, 398–401 . doi:10.1038/nature13957pmid:25409830

15. Graven, H. D., Keeling, R. F., Piper, S. C., et al. (2013). *Enhanced seasonal exchange of $CO_2$ by northern ecosystems since 1960*. *Science* , **341**, 1085–1089.

16. Horn, J. E., Schulz, K. (2011). **Identification of a general light use efficiency model for gross primary production,** *Biogeosciences*, **8** , 999-1021.

17. Huang, M., Piao, S., Ciais, P., Peñuelas, J., Wang, X., Keenan, T. F., Peng, S., Berry, J. A., Wang, K., & Mao, J. (2019). Air temperature optima of vegetation productivity across global biomes. *Nature ecology & evolution*, **1**.

18. Jiang, M., Medlyn, B., Drake J., et al. (2020). The fate of carbon in a mature forest under carbon dioxide enrichment. Nature, 580, 227-231.

19. Jung, M., Reichstein, M., Schwalm, C. R., et al. (2017). Compensatory water effects link yearly global land $CO_2$ sink changes to temperature. *Nature*, **541**( 7638), 516– 520.

20. Kauppi, P. and Posch, M. (1985). Sensitivity of boreal forests to possible climatic warming. Climatic Change. **7(1)**, 45-54.

21. Keeling, C. D., Harris, T. B., and Wilkins, E. M. (1968). Concentrations of atmospheric carbon dioxide at 500 and 700 millibars, *J. Geophys. Res*. **73**, 4511–4528 (1968).

22. Keenan, T. F. and Riley, W. J. (2018). Greening of the land surface in the world's cold regions consistent with recent warming. Nature Climate Change, **8**(9), 825–828.

23. Kharuk, V., Ranson, K. J., Dvinskaya, M. L. (2007). Evidence of evergreen conifer invasion into larch dominated forests during recent decades in central Siberia. Eurasian *J. For. Res.* **10**, 163–171.

24. **Kimball, B. A. (1983).** Carbon-dioxide and agricultural yield. An assemblage and analysis of 430 prior observations. *Agron. J.* **75**, 779–88.

25. Li, X., Xiao, J., He, B. (2018). Chlorophyll fluorescence observed by OCO-2 is strongly related to gross primary productivity estimated from flux towers in temperate forests. *Remote Sensing of Environment*, **204**, 659-671.

26. Liu, J., Bowman, K. W., Lee, M., et al. (2014). Carbon monitoring system flux estimation and attribution: impact of ACOS-GOSAT XCO2 sampling on the inference of terrestrial biospheric sources and sinks. *Tellus B*, **66**, May. Available at: <http://www.tellusb.net/index.php/tellusb/article/view/22486>

27. Liu, J., Bowman, K. W., Schimel, D. S., et al. (2017). *Contrasting carbon cycle responses of the tropical continents to the 2015–2016 El Nino. Science, 358 eaam5690.*

28. Liu, J., Bowman, K W., Parazoo, N. C., et al. (2018). Detecting drought impact on terrestrial biosphere carbon fluxes over contiguous US with satellite observations, *Environmental Research Letters*, **13**, 095003 (2018).

29. Long, S. P., Ainsworth, E. A., Rogers, A., Ort, D. R. (2004). Rising atmospheric carbon dioxide: plants FACE the future. Annual Review of Plant Biology, **55**, 591–628.

30. Menemenlis, D., Campin, J.M., Heimbach, P., Hill, C., Lee, T., Nguyen, A., Schodlok, M., Zhang, H. (2008). ECCO2: High resolution global ocean and sea ice data synthesis. *Mercator Ocean Quarterly Newsletter.* **31**, 13–21 .

31. Natali, S. M., Watts, J. D., Rogers, B. M., et al. (2019). Large loss of CO2 in winter observed across the northern permafrost region. *Nature Climate Change*, ***9***(11), 852-857.

32. Nemani, R. R., Keeling, C. D., Hashimoto, H., et al. (2003). Climate-driven increases in global terrestrial net primary production from 1982 to 1999. *Science* **300**, 1560–1563.

33. Oda, T., Maksyutov, S., Andres, R. J. (2018). The Open-source Data Inventory for Anthropogenic $CO_2$, version 2016 (ODIAC2016): a global monthly fossil fuel $CO_2$gridded emissions data product for tracer transport simulations and surface flux inversions, *Earth Syst. Sci. Data*, doi:10.5194/essd-10-87-2018,.

34. Parazoo, N. C., Bowman, K. W., Fisher, J. B., et al. (2014). Terrestrial gross primary production inferred from satellite fluorescence and vegetation models. *Glob Change Biol*, **20**: 3103-3121. doi:10.1111/gcb.12652

35. Park, T., Ganguly, S., Tømmervik H., et al. *(2016).* **Changes in growing season duration and productivity of northern vegetation inferred from long-term remote sensing data.** *Environ. Res. Lett.,* **11** , Article 084001.

36. Piao, S., Liu, Z., Wang, Y., et al. (2018). On the causes of trends in the seasonal amplitude of atmospheric $CO_2$. *Glob Change Biol*. **24**, 608– 616. https://doi.org/10.1111/gcb.13909.

37. Randerson, J. T., Thompson, M. V., Conway, T. J., Fung, I. Y. , Field, C. B. (1997). The contribution of terrestrial sources and sinks to trends in the seasonal cycle of atmospheric carbon dioxide, *Global Biogeochem. Cycles*, **11**( 4), 535– 560.

38. Schimel, D. S., Braswell, B. H., Parton, W. J., (1997). Equilibration of the terrestrial water, nitrogen, and carbon cycles. *Proceedings of the National Academy of Sciences*, **94**, 8280-8283.

39. Schimel, D., Pavlick, R., Fisher, J. B., et al. (2015). Observing terrestrial ecosystems and the carbon cycle from space. Glob Change Biol, **21**: 1762-1776. doi:10.1111/gcb.12822

40. Schuur, E. A. G., McGuire, A. D., Schadel, C., et al. (2015). Climate change and the permafrost carbon feedback. *Nature* **520**, 171–179.

41. Sitch, S., Friedlingstein, P., Gruber, N., et al. (2015). Recent trends and drivers of regional sources and sinks of carbon dioxide, *Biogeosciences*, **12**, 653–679, https://doi.org/10.5194/bg-12-653-2015.

42. Sun, Y., Frankenberg, C., Jung, M., et al. (2018). Overview of Solar-Induced chlorophyll Fluorescence (SIF) from the Orbiting Carbon Observatory-2: Retrieval, cross-mission comparison, and global monitoring for GPP. Remote Sensing of Environment, **209**, 808-823. https://doi.org/10.1016/j.rse.2018.02.016

43. Sullian et al. (2020). Long-term thermal sensitivity of Earth's tropical forests. *Science,* 368, 869-874 DOI: 10.1126/science.aaw7578

44. Tramontana, G., Jung, M., Schwalm, C. R. (2016). Predicting carbon dioxide and energy fluxes across global FLUXNET sites with regression algorithms. *Biogeosciences*, **13,** 4291– 4313.

45. Wang, J. A., Sulla-Menashe, D., Woodcock, C. E., et al. (2019). Extensive land cover change across Arctic–Boreal Northwestern North America from disturbance and climate forcing. *Glob Change Biol*., **00**, 1– 16. https://doi.org/10.1111/gcb.14804

46. Welter, J. R., Benstead, J. P., Cross, W. F., et al. (2015). Does $N_2$ fixation amplify the temperature dependence of ecosystem metabolism?.*Ecology*, **96**, 603-610. doi:10.1890/14-1667.1

47. Wofsy, S. C., HIPPO Science Team and Cooperating Modellers and Satellite Teams, (2011). HIAPER Pole-to Pole Observations (HIPPO): fine-grained, global-scale measurements of climatically important atmospheric gases and aerosols. *Philos. Trans. R Soc. A* **369,** 2073–2086.

48. Yuan, W., Luo, Y., Liang, S., et al. (2011). Thermal adaptation of net ecosystem exchange, *Biogeosciences*, **8**, 1453–1463, https://doi.org/10.5194/bg-8-1453-2011.

49. Zeng, N., Zhao, F., Collatz, G. J., et al. (2014). Agricultural green revolution as a driver of increasing atmospheric $CO_2$ seasonal amplitude. *Nature,* **515***,* 394–397 . doi:10.1038/nature13893pmid:2540982.

50. Zhao, F. and Zeng, N. (2014). Continued increase in atmospheric $CO_2$ seasonal amplitude in the 21st century projected by the CMIP5 Earth system models*, Earth Syst. Dynam*., **5**, 423–439. https://doi.org/10.5194/esd-5-423-2014, 2014.

51. Zhu, Z., Piao, S., Myneni, R. B., et al. (2016). Greening of the Earth and its drivers. *Nat. Clim. Change,* **6**, 791–795.

52. Zhu, Z., Bi, J., Pan, Y., et al. (2013). Global Data Sets of Vegetation Leaf Area Index (LAI)3g and Fraction of Photosynthetically Active Radiation (FPAR)3g Derived from Global Inventory Modeling and Mapping Studies (GIMMS) Normalized Difference Vegetation Index (NDVI3g) for the Period 1981 to 2011. *Remote Sens.,* ***5***, 927-948.